

## Interdigital *H*-mode drift-tube linac design with alternative phase focusing for muon linac

M. Otani,<sup>\*</sup> T. Mibe, and M. Yoshida

*High Energy Accelerator Research Organization (KEK), Ibaraki 305-0801, Japan*

K. Hasegawa and Y. Kondo

*Japan Atomic Energy Agency (JAEA), Tokai, Naka, Ibaraki 319-1195, Japan*

N. Hayashizaki

*Tokyo Institute of Technology, Tokyo 152-8550, Japan*

Y. Iwashita

*Kyoto University, Kyoto 611-0011, Japan*

Y. Iwata

*National Institute of Radiological Sciences (NIRS), Chiba 263-8555, Japan*

R. Kitamura

*University of Tokyo, Hongo 113-8654, Japan*

N. Saito

*J-PARC Center, Tokai, Naka, Ibaraki 319-1195, Japan*

(Received 16 February 2016; published 25 April 2016)

We have developed an interdigital H-mode (IH) drift-tube linac (DTL) design with an alternative phase focusing (APF) scheme for a muon linac, in order to measure the anomalous magnetic moment and electric dipole moment (EDM) of muons at the Japan Proton Accelerator Research Complex (J-PARC). The IH-DTL accelerates muons from  $\beta = v/c = 0.08$  to 0.28 at an operational frequency of 324 MHz. The output beam emittances are calculated as  $0.315\pi$  and  $0.195\pi$  mm mrad in the horizontal and vertical directions, respectively, which satisfies the experimental requirement.

DOI: 10.1103/PhysRevAccelBeams.19.040101

### I. INTRODUCTION

The design of an interdigital H-mode (IH) drift-tube linac (DTL) for the acceleration of low-velocity protons was first proposed in 1956 [1], and this concept has been studied throughout the intervening decades [2,3]. One remarkable research achievement is the IH-DTL for hadron therapy that employs the alternating phase focusing (APF) method [4,5]. The APF method facilitates simultaneous focusing in the transverse and longitudinal directions, in addition to a high accelerating field gradient. Further, the complex APF cavity design is now manageable, as a result of recent enhancements to computational power; thus three-dimensional electromagnetic fields can be considered. IH-DTL applications have been extended to the

acceleration of a variety of particles, such as heavy ions [6,7]. This paper describes the first attempt to adopt the APF IH-DTL for a low-emittance muon beam.

Low-emittance muon beams offer new research opportunities that have implications for several scientific fields [8–11]. One noteworthy application is in the search for new physics beyond the standard model (SM) of elementary particle physics. A difference of approximately three standard deviations exists between the SM prediction and the measured value (with a precision of 0.54 ppm) of the muon anomalous magnetic moment  $(g-2)_\mu$  [12]. This discrepancy is thought to be due to interactions or particles that are unknown to the SM; therefore, further investigations are desired. Low-emittance muon beams will facilitate more precise measurements, as the dominant systematic uncertainties in the previous experimental results are due to the muon beam dynamics in the muon storage ring.

At present, we are developing a muon linac for the  $(g-2)_\mu$  experiment at the Japan Proton Accelerator Research Complex (J-PARC) [13], in order to realize a low-emittance muon beam. In the experiment, ultra slow muons with an

<sup>\*</sup>masashio@post.kek.jp

Published by the American Physical Society under the terms of the *Creative Commons Attribution 3.0 License*. Further distribution of this work must maintain attribution to the author(s) and the published article's title, journal citation, and DOI.

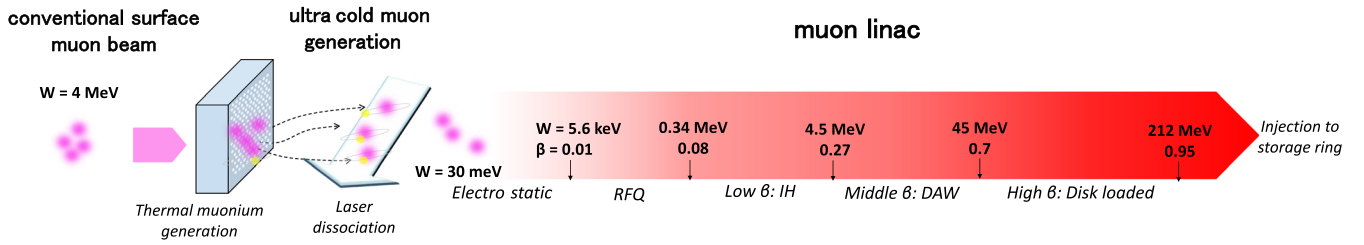


FIG. 1. Configuration of low-emittance muon beam.

extremely small transverse momentum of 3 keV/c (kinetic energy  $W = 30$  meV) are generated via thermal muonium production [14] followed by laser dissociation [15]. The generated ultra slow muons are electrostatically accelerated to  $\beta = v/c = 0.01$  (5.6 keV) and injected into the muon linac.

Figure 1 shows the muon linac configuration. In order to obtain a longitudinally bunched beam, a radio-frequency-quadrupole (RFQ) accelerator is employed for the first-stage acceleration. The operational frequency is chosen to be 324 MHz, in order to optimize the experiences at the J-PARC H<sup>-</sup> RFQ [16]. Although conventional linacs adopt Alvarez DTLs after RFQs, an H-mode DTL is employed during the particle velocity  $\beta = 0.08$  to 0.28 (4.5 MeV) stage, so as to yield a higher acceleration efficiency. After the muon is accelerated to  $\beta = 0.28$ , a disk-and-washer (DAW) -type coupled cavity linac (CCL) with an operational frequency of 1.3 GHz is employed for effective acceleration [17]. Because the  $\beta$  variation is modest in the high- $\beta$  region, the design emphasis has been shifted to achieving a high accelerating gradient, in order to realize a sufficiently short distance. Therefore, a disk-loaded structure is used for  $\beta$  is greater than 0.7 (42 MeV).

In order to satisfy the experimental requirement of an extremely small transverse divergence angle of  $10^{-5}$ , the muon should be accelerated to a momentum of 300 MeV/c (212 MeV), without substantial emittance growth. In addition, the effective accelerating gradient should be relatively high, especially in the low  $\beta$  region (less than 0.28), in order to avoid muon decay loss due to the muon finite lifetime of  $2.2\mu\text{s}$ . Moreover, the construction cost is desirable to be reduced. Based on these considerations, an IH DTL incorporating the APF method is employed for the acceleration stage from  $\beta = 0.08$  to 0.28.

There are two candidates for the room-temperature H-mode structure. One is an IH staccator. In the heavy ion accelerator structure that works in the TE<sub>11</sub>-mode, while the other is a crossbar H-mode (CH) operated in the TE<sub>21</sub>-mode [18]. Because the CH and IH structures have comparable acceleration efficiency [19], and because the IH structure is able to be fabricated at lower cost using a three-piece design in which two semicylindrical shells are attached to a center frame [20,21], an IH structure is employed.

An IH DTL has preciously been utilized for a heavy-ion accelerator. In the heavy-ion accelerator the transverse

focusing is provided by magnetic quadrupoles in a focusing section [22]. However, insertion of the focusing sections increased the accelerator length and, hence, caused additional decay loss. One solution involves the use of an H-mode accelerating structure with permanent-magnet quadrupole (PMQ) magnets in the drift tubes [23]. However, although this setup provides sufficient transverse focusing, the production cost is increased. As a sufficient focusing force and a reduced production cost are desirable, APF is the dominant candidate; in this approach, the transverse and longitudinal focusing are achieved with the rf field only, and no additional focusing element is necessary. Although the APF is limited to a small current beam, as a result of the weak transverse focusing field, it can be applied in a muon linac, because the proposed intensity of the ultracold muon beam is very small ( $\sim 10^6$  muons per second with 25 bunches).

In this paper, we describe the design of the APF IH-DTL for the J-PARC experiment in detail. The paper is structured as follows. In Sec. II, the APF IH-DTL design procedures are described. Section III is devoted to results obtained using the optimized design and related discussion. The conclusions are presented in Sec. IV.

## II. APF IH-DTL DESIGN

In the APF scheme, the gap-to-gap synchronous phases are varied in order to achieve longitudinal and transverse focusing. However, the synchronous phase array determines each cell length and changes the average on-axis field  $E_0$  at each gap, which in turn affects the particle motion. Hence, the phase array optimization is strongly correlated to the beam dynamics and the cavity design. In order to solve this convoluted problem, the procedure is divided into the following three steps:

### (A) Synchronous phase array optimization

The synchronous phases for each cell are optimized in order to obtain an improved output beam. In this step, the beam dynamics are calculated analytically using certain approximations, and the  $E_0$  at each gap is assumed to be constant.

### (B) Cavity optimization

In the optimized phase array, the cells are aligned in the IH cavity. Then, the other geometries of the cavity, such as the shape of the ridge end cuts, are adjusted in order to achieve a flat electric field.

## (C) Particle tracking

Using the calculated field with the optimized cavity, the three-dimensional trajectory and energy gain are calculated numerically.

Details of each step are explained in Secs. II A, II B, and II C, respectively.

**A. Synchronous phase array optimization**

In this step, the particle dynamics are calculated analytically using certain approximations and for a particular synchronous phase array. These calculations are performed using LINACSapf [24], with some modifications for the dynamics calculations and the synchronized phase array definition to accommodate the  $\pi$ -mode acceleration, whereas  $2\pi$ -mode acceleration is assumed in the original code.

The particle dynamics are calculated using a simple matrix, in which each cell is represented as a drift and a rf gap. The cell length is determined by the phase difference across the cells and by  $\beta$ , as shown in Fig. 2. Here, the synchronous phase for cell number  $n$  is represented by  $\phi_n$ . The wavelength is labeled  $\lambda$ , while the gap length is labeled  $g$ ; this is fixed to  $0.2 \times \beta\lambda$  in the study. In the original LINACSapf code, two drift tubes and gaps are defined as a single cell, and a synchronous phase is assigned to each cell with this definition.

The transit time factor  $T$  is approximated by the square profile of the electric field [25,26]:

$$T = \frac{1}{I(k\sqrt{1-\beta^2}a)} \frac{\sin(\pi g/\beta\lambda)}{\pi g/\beta\lambda}, \quad (1)$$

where  $I$  is the modified Bessel function of the 0-th order,  $k = 2\pi/\beta\lambda$ , and  $a$  is the bore radius. The Bessel function is added to the original LINACSapf code in order to account for the effects of  $a$ .

The energy gain in gap  $n$  ( $\Delta W_n$ ) is calculated from

$$\Delta W_n = qV_0 T \cos \phi_n, \quad (2)$$

where  $q$  is the electric charge and  $V_0$  is the axial rf voltage defined by  $E_0 g \beta \lambda$ .  $E_0$  is determined from the Kilpatrick criterion [27,28]. The Kilpatrick limit  $E_{\text{kilpat}}$  at 324 MHz is 17.8 MV/m and a value of approximately  $1.8 \times E_{\text{kilpat}}$  is employed for the maximum surface field, based on the empirical value applying to RFQs. Assuming that the peak-to-average ratio is three,  $E_0$  is set to 10 MV/m.

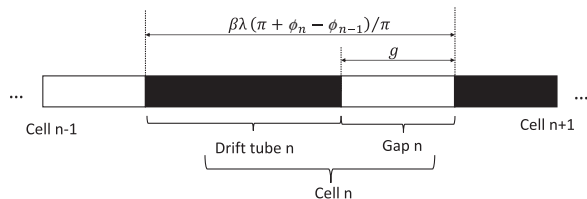


FIG. 2. Cell arrangement in accordance with synchronous phase.

The maximum surface field will be confirmed following discussion of the cavity design in Sec. II B. Here, the  $E_0$  values for all cells are assumed to be identical, because this is preferable in terms of power consumption, heat generation, and electric discharge.

As for the transverse momentum kick, not only the rf-defocusing force, but also the radial displacement and the electrostatic focusing are considered, because the beta change in each cell is large. Thus, the transverse momentum kick is expressed as [25]

$$\Delta(\gamma\beta r') = -\frac{q}{2mc^2} E_g \left\{ \frac{r_1}{\beta_1} \cos\left(\frac{\pi g}{\beta\lambda} - \phi\right) - \frac{r_2}{\beta_2} \cos\left(\frac{\pi g}{\beta\lambda} + \phi\right) \right\}, \quad (3)$$

where 1 and 2 refer to the entrance and exit positions of the gap, respectively. The radial displacement and muon mass are labeled  $r$  and  $m$ , respectively. Only the rf-defocusing force is implemented in the original “LINACSapf” code; therefore, that part of the code is replaced with Eq. (3).

In the code, the dimensions of the drift tubes and gaps are calculated with assigned  $E_0$ , the particle velocity of the central orbit, and assigned synchronous phase array  $\{\phi_n\}$ . Then the dynamics of all the particles are calculated. The initial settings of the synchronized phase array are assigned based on those for the HIMAC accelerator [6]. All the  $\{\phi_n\}$  are optimized using the minimization function  $f$ , which is defined based on the emittance growth ( $\Delta\epsilon$ ), the energy spread of the output beam ( $\Delta E$ ), and the loss particle efficiency ( $\epsilon_{\text{loss}}$ ), such that  $f = \Delta\epsilon + \Delta E + \epsilon_{\text{loss}}$ . The NPSOL minimization algorithm [29] implemented in LINACSapf is used for the optimization. NPSOL is a set of Fortran subroutines for minimizing a smooth function subject to constraints. The result described below was confirmed with several iterations where the initial parameters and the parameter constraints were changed.

The output energy is set to approximately 4 MeV and corresponds to 16 cells. The cavity length is calculated to be approximately 1.3 m. Note that cavities with this length is able to be produced at low cost.

Figure 3 shows the optimized phase array results. Gap numbers 1–2, 6–9, 15 and 16 have negative synchronous phases, during which time the beam is longitudinally focused. However, gap numbers 3–5 and 10–14 have positive, during which time the beam is transversely focused. Because the electrostatic focusing [as described in Eq. (3)] is stronger in the lower-beta part, the first collection of positive phase groups has a smaller number of gaps. Table I shows details of the optimized parameters. The output energy is 4.5 MeV.

**B. IH cavity optimization**

Because the IH cavity is not axially symmetric, a three-dimensional model is necessary in order to evaluate the

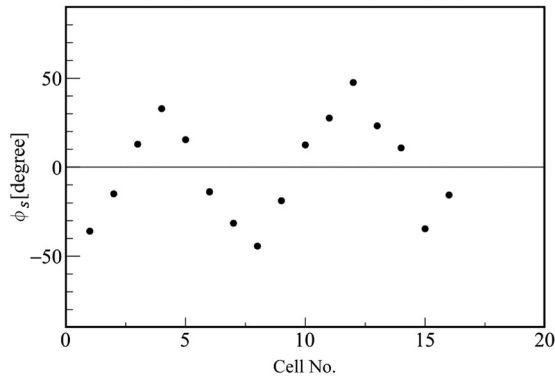


FIG. 3. Optimized phase ( $\phi_s$ ) array results as function of cell (gap) number.

electromagnetic field. In addition, the electromagnetic field and the resonant frequency depend on the entire structure of the IH cavity, and the detail of the overall structure (including the ridges, etc.) should thus be incorporated in the calculation model. Therefore, the entire IH cavity is modeled using the CST Micro Wave (MW) Studio [30] three-dimensional field solver, in order to calculate the electromagnetic field. Figure 4 shows the three-dimensional model of the IH cavity in CST MW Studio. The IH cavity consists of a cylindrical cavity and two ridges mounted on either the top or bottom of the cavity. To operate the IH cavity as an accelerator in the  $TE_{11}$ -mode, drift tubes are mounted alternately on the top and bottom ridges via stems. The stems are connected to the drift tubes at their centers, and end ridge-cuts are present in the top and bottom ridges (ridge tuners). The inner radius of the cavity is tapered in the down- to upstream (cavity taper) direction. The ridge tuner shape and the cavity taper are varied in order to adjust the flatness of the electric field.

TABLE I. Cell parameters for optimized phase array.

Cell	W [MeV]	$\beta$	$\phi$ [degrees]	Cell length [mm]	Total length [mm]
1	0.34	0.08	-35.9	29.5	29.5
2	0.43	0.09	-14.9	46.0	75.4
3	0.57	0.10	12.9	54.9	130
4	0.74	0.12	32.9	60.3	191
5	0.92	0.13	15.4	54.4	245
6	1.14	0.15	-13.8	56.0	301
7	1.38	0.16	-31.4	66.4	367
8	1.63	0.17	-44.3	74.1	442
9	1.86	0.19	-18.8	97.2	539
10	2.16	0.20	12.5	108	646
11	2.49	0.21	27.6	106	753
12	2.82	0.23	47.6	116	868
13	3.10	0.24	23.2	94.2	963
14	3.50	0.25	10.8	108	1070
15	3.95	0.27	-34.6	91.5	1160
16	4.30	0.28	-15.6	142	1300
exit	4.50				

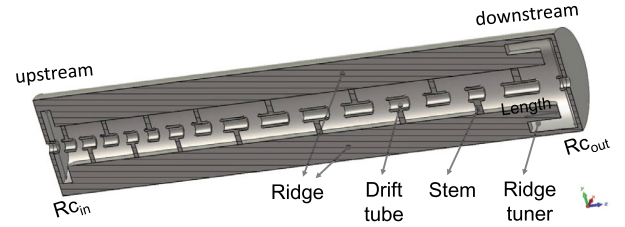


FIG. 4. Three-dimensional model of IH cavity in CST MW Studio calculation.

To optimize the IH cavity, the drift tubes and the acceleration gaps are first arranged according to the previously determined optimized parameters shown in Table I. Other dimensions, such as the ridges and stems, are implemented on the basis of previous prototype production experience [21]. Because the drift tube length and  $g$  depend on both the synchronous phase and beta, the inductance and capacitance along the cavity are not constant, which distorts the acceleration field. In order to achieve flat electric field on the beam axis  $E_z$ , the following dimensions are adjusted: the cavity radius, the ridge tuner length, the cavity taper, the stem radius, and the tube radius.

Note that adjustment of the cavity radius is used to tune the resonant frequency, and the radius tuning does not strongly influence the  $E_z$  flatness. The flatness is first optimized through tuning of the other parameters; the resonant frequency is then adjusted by changing the cavity radius.

The  $E_z$  flatness is primarily tuned using the ridge tuner and the cavity taper. The black and blue lines in Fig. 5 show the longitudinal electric field along the beam axis before and after these optimizations. Before the optimizations,

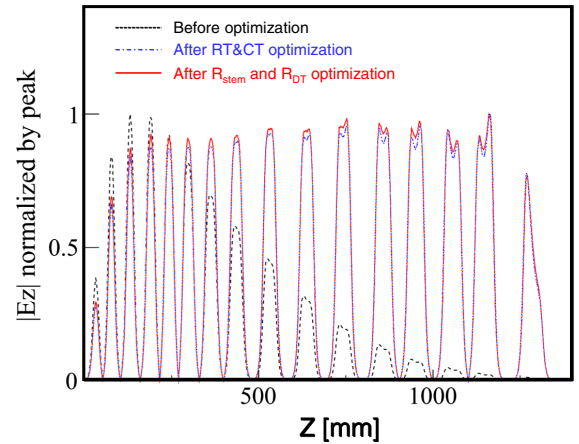


FIG. 5. Effects of ridge tuner (RT), cavity taper (CT), stem radius ( $R_{stem}$ ), and drift tube radius ( $R_{DT}$ ) adjustment. Horizontal axis is the distance from the cavity start on the beam axis, and vertical axis is the  $E_z$  normalized at the peak value. Black: longitudinal electric field along  $z$  before optimizations, blue: field after optimizations with RT and CT, red: field after optimizations with  $R_{stem}$  and  $R_{DT}$ .

the field in the downstream region is lower than that in the upstream region, because the acceleration gaps in the downstream region are smaller than those upstream, and the equivalent capacitance gradient results in a field gradient. The tilting field is prescribed by adjusting the ridge tuner length and the cavity taper.

Fine tuning of  $E_z$  in each gap is achieved by changing the stem radius and the drift tube radius, as shown by the red line in Fig. 5. By first adjusting the radius and then varying the equivalent inductive load at each gap, the field differences between the gaps can be corrected. Because the stem radius and the drift tube radius are correlated with the feasibility of the manufacturing process, the range of adjustment is feasible in terms of manufacturing.

The cavity parameters obtained through the optimization process are summarized in Table II. The variation in the electric field in the gaps is approximately 10%, excluding the first and last cells. The resonant frequency is tuned to a slightly lower value than the 324-MHz operation frequency, in order to leave room for the tuner knobs with the inductive tuner installed on the cavity side wall. The quality factor ( $Q_0$ ) is calculated to be  $1.07 \times 10^4$ . The effective shunt impedance is calculated to be 92 M $\Omega$ /m, and the operation power is required to be 250 kW. The effective shunt impedance is competitive to those of other IH structures given our IH application to relatively higher velocity region.

The maximum surface field is evaluated to be 34 MV/m at the outer surface of the most downstream drift tube, corresponding to 1.9 times the Kilpatrick limit. This value is reasonable based on the experiences in RFQs. Further

TABLE II. Dimensions and parameters of optimized IH cavity. The cavity radii at the down- and upstream ends are labeled  $R_{c_{out}}$  and  $R_{c_{in}}$ , respectively. The ridge tuner length, the stem radius, and the drift tube radius are labeled  $L_{RT}$ ,  $R_{stem}$ , and  $R_{DT}$ , respectively.

$R_{c_{out}}$ [mm]	$R_{c_{in}}$ [mm]	$L_{RT}$ [mm]	Cell#	$R_{stem}$ [mm]	$R_{DT}$ [mm]
			1	17.1	5
			2	17.2	5
			3	16.6	5
			4	16.7	5
			5	17.6	5
			6	17.8	5
			7	17.9	5
			8	18	6
129	96.9	85	9	18.1	7
			10	18.05	7
			11	18.15	7
			12	18.5	7
			13	18.1	6.75
			14	18.8	8.5
			15	18.4	9
			16	18.9	8

reduction of the maximum field will be attained through optimization of the chamfered structure at the edge of the drift tube.

### C. Particle tracking

Next the beam particle trajectory is simulated using the general particle tracer (GPT) [31]. In GPT, the dynamics is calculated with an embedded fifth order Runge-Kutta driver with the sufficiently small step size. The electric and magnetic fields calculated using CST MW Studio are implemented in the code and the particle dynamics are calculated numerically. The number of simulated particles is  $10^5$  that corresponds to designed muon beam intensity per bunch.

Figure 6 (top) shows the normalized velocity in the  $x$ -direction along the beam axis ( $z$ ) with overwriting of the synchronous phase ( $\phi$ ). As shown in the red hatched box in Fig. 6, the synchronous phases are positive for  $z = 130\text{--}250$  mm and  $650\text{--}1070$  mm, where the transverse focusing is implemented. During these periods, the horizontal velocity is decreased.

Figure 6 (bottom) shows the normalized velocity in the  $y$ -direction along the beam axis. The vertical trajectory is dominated by the finite value of the vertical electric field.

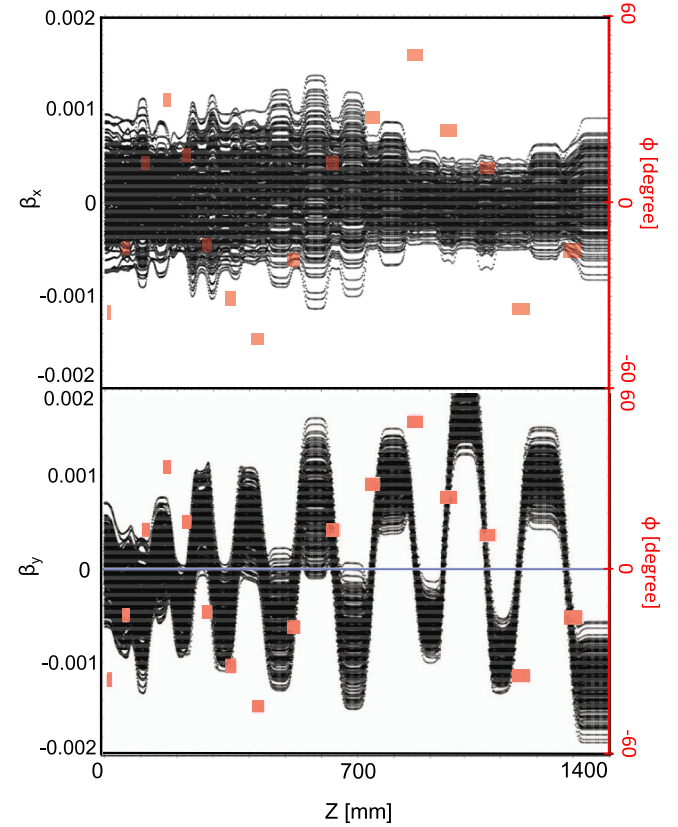


FIG. 6. Beam velocity distribution as a function of distance along the IH structure (black) and synchronous phase in each position (red).  $\beta_x$  (top) and  $\beta_y$  (bottom) along beam axis.

In order to reduce the additional growth, some conventional solutions, such as the use of drift tube bulges [23], have been considered. However, this approach only reduces the vertical field by a small number of percentage points because the cell length is relatively large (because of the application of the IH structure to yield a higher  $\beta$  region). As a result, no sufficient suppression of the extra growth is achieved using these the additional structures. Because the extra growth is acceptably small and the output beam satisfies the requirement of the J-PARC  $g - 2/\text{EDM}$  experiment (where EDM is “electric dipole moment”), no additional structures are implemented in this design, so as to avoid additional power loss at these structures.

### III. RESULTS AND DISCUSSION

The output beam with the optimized IH design was evaluated, and the results are discussed in this section.

First, the output beam from the IH was evaluated using the analytical method described in Sec. II A. In this evaluation, the input beam distributions were assumed to be of water-bag (wb) type. The transverse emittance growths were calculated to be approximately  $0.02\pi$  mm mrad, and are considered to be due to the nonlinear focusing generated by the APF scheme.

Second, the emittance growths with the realistic rf fields were evaluated using numerical calculations, as discussed in Sec. II C. In this evaluation, the input beam distributions were assumed to be of wb type. Figure 7 shows the emittance growth along the beam axis, and indicates that the emittance growth in the y-direction is primarily generated in the last cell. This is due to the  $\vec{\beta} \times \vec{H}$  kick in the last cell, which is relatively large in our case because of the application of the IH structure to the relatively large velocity region ( $\beta = 0.28$ ). In the absence of this effect, the emittance growths in the x- and y-directions are consistent

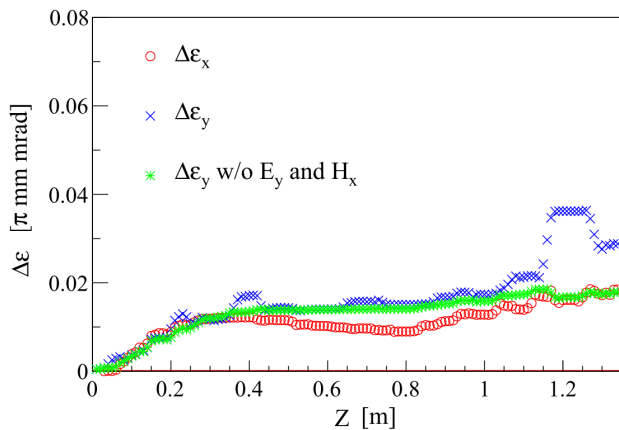


FIG. 7. Emittance growth ( $\Delta\epsilon$ ) along beam axis ( $z$ ). Red: emittance growth in the x-direction ( $\Delta\epsilon_x$ ), blue: emittance growth in the y-direction ( $\Delta\epsilon_y$ ), green: emittance growth in the y-direction without the vertical electric field ( $E_y$ ) and the horizontal magnetic field ( $H_x$ ).

with those in the analytical evaluation, within the range of a few percent. Because the peak current of the muon beam is low and then the space charge effects are negligible, the results are consistent between the analytical evaluation in which the space charge effects are not implemented and the numerical calculation in which the space charge effects taken into account.

Finally, the most precise evaluation of the output beam can be obtained using realistic input beam distributions. The input beam was obtained from simulations of the surface muon beamline, the ultra slow muon system, and the RFQ [32]. From the results, the normalized root mean square (rms) emittances of the input beam were evaluated as  $0.297\pi$  mm mrad in the x-direction,  $0.168\pi$  mm mrad in the y-direction, and  $0.0181\pi$  MeV deg in the z-direction. Because the structure is not periodic due to the APF method and rapidly changing velocity profile, the twiss parameters ( $\alpha$  and  $\beta$ ) at the IH entrance were scanned in order to obtain a matching condition to the IH, instead of the conventional method solving a periodic solution of the transfer matrix. Based on the scan results, the transport line from the RFQ to the IH was designed using TRACE3D [33], and the beam distributions at the RFQ exit were then transported using PARMILA [34]. Figure 8 shows the calculated phase-space distributions of the output beam. The emittance growth was calculated to be  $0.018\pi$  (6.1%) and  $0.027\pi$  mm mrad (16%) in the x- and y-directions, respectively. This is consistent with the evaluations using the wb distribution to within a few percent, and the small discrepancy is due to the difference in the distribution shape in the z-direction. The output beam distributions are improved from those in early work [21] with developments for the

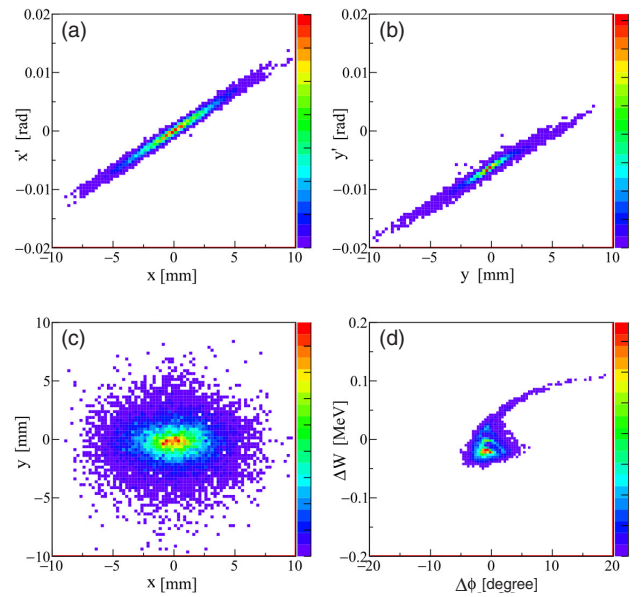


FIG. 8. Calculated phase space distributions at IH exit. (a) the horizontal divergence angle  $x'$  vs  $x$ , (b) the vertical divergence angle  $y'$  vs  $y$ , (c)  $y$  vs  $x$ , and (d)  $\Delta W (W = 4.5 \text{ MeV})$  vs  $\Delta\phi$ .

TABLE III. Summary of simulation output beam parameters. Output with wb: The input beam distribution is wb-type with assigned emittance. output RFQ: The RFQ output beam distributions are used as the input beam.

	Input	Output with wb	RFQ
$\beta$	0.08	0.28	←
Energy (MeV)	0.34	4.49	←
$\varepsilon_x$ [ $\pi$ mm mrad]	0.297	0.315	0.315
$\varepsilon_y$ [ $\pi$ mm mrad]	0.168	0.197	0.195
$\varepsilon_z$ [ $\pi$ MeV deg]	0.0181	0.0224	0.0303
Transmission [%]			99.9
Beam transit time [nsec]			25
Survival rate [%]			98.9
Transmission total [%]			98.7

optimization method of the synchronous phase array (Sec. II A) and the IH cavity model (Sec. II B). The transmission efficiency without any selections in output beam was calculated to be 99.9%. Some particles in the longitudinal tail component are difficult to be accelerated by following DAW structure. In order to estimate the expected impact on the transmission of the following DAW structure, the transmission is estimated with  $|\Delta W| < 0.05$  MeV. The transmission is 98.1% and it is sufficiently small. The beam transit time  $t_{\text{tran}}$  was 25 ns and the muon survival rate is calculated to be  $\exp(t_{\text{tran}}/\tau_\mu \bar{\gamma}) = 98.9\%$ , where the average Lorentz factor during acceleration is labeled  $\bar{\gamma}$ . The total transmission is expected to be 98.7%, which is sufficient for the  $g - 2/\text{EDM}$  experiment.

Table III summarizes the particle simulation results. The output emittance was estimated to be  $0.315\pi$  and  $0.195\pi$  mm mrad in the horizontal and vertical directions, respectively, and the emittance growths were sufficiently small in the APF-IH DTL. Because the following rf cavities consist of conventional linac structures (DAW and disc loaded structure), the emittance growth is expected to be acceptably small. Therefore, the beam emittance will meet the requirement for the J-PARC  $g - 2/\text{EDM}$  experiment.

As the beam stability in the APF scheme depends on the rf field only, the beam dynamics may be affected by errors in the gap fields. To estimate this effect, the beam dynamics were simulated by changing the fields from the nominal values by several percent. As a result, the additional emittance growth due to the field fluctuations was estimated to be several percent for a field variation of 1%, which is a conservative value for the conventional rf power system. Note that the actual field fluctuation will be significantly smaller than 1%.

#### IV. CONCLUSION

In this paper, the systematic procedures employed in order to optimize the APF IH-DTL design for the J-PARC  $g - 2/\text{EDM}$  experiment were presented. First, the synchronous phase array was optimized in order to obtain lower

emittance growth, using analytical calculations of the beam dynamics. Then, the IH cavity dimensions were tuned in order to obtain both an optimized phase array and field flatness, using finite element method calculation. Finally, the beam dynamics obtained for the calculated rf fields was evaluated via numerical calculations.

According to these procedures, the APF IH-DTL design is suitable for the muon linac in the J-PARC  $g - 2/\text{EDM}$  experiment. The beam emittance after the APF IH-DTL was calculated to be  $0.315\pi$  and  $0.195\pi$  mm mrad in the x- and y-directions, respectively. In order to satisfy the J-PARC  $g - 2/\text{EDM}$  experimental requirement, the emittance growth during the acceleration should be as small as possible. Here, the emittance growth in the APF IH-DTL was evaluated to be 6% and 16% in the x- and y-directions, respectively. As the following rf cavities consist of conventional structures, substantial emittance growth is not expected. In conclusion, the designed APF IH-DTL satisfies the J-PARC  $g - 2/\text{EDM}$  experimental requirement.

#### ACKNOWLEDGMENTS

The authors are grateful to R. A. Jameson for useful advice on the APF linac and on modifications of the LINACs<sub>apf</sub> code. We would like to thank the KEK staff for their support. This work was supported by JSPS KAKENHI Grant No. 15H03666.

- 
- [1] J. P. Blewett, *Symposium du CERN sur les Accelérateurs de Haute Énergie et la Physique des Mesons  $\pi$  v.1*, Regenstreif and Edouard (CERN, Geneva, 1956), p. 162.
  - [2] P. M. Zeidlitz and V. A. Yamnitskii, Accelerating systems employing *H*-type waves, *J. Nucl. Energy, Part C* **4**, 121 (1962).
  - [3] J. Pottier, A new structure for heavy-ions linacs, *IEEE Trans. Nucl. Sci.* **16**, 377 (1969).
  - [4] M. L. Good, Phase-reversal focusing in linear accelerators, *Phys. Rev.* **92**, 538 (1953).
  - [5] S. Minaev and U. Ratzinger, APF or KONUS drift tube structures for medical synchrotron injectors - A comparison, in *Proceedings of the 18th Particle Accelerator Conference, New York, 1999* (IEEE, New York, 1999).
  - [6] Y. Iwata *et al.*, Alternating-phase-focused IH-DTL for an injector of heavy-ion medical accelerators, *Nucl. Instrum. Methods Phys. Res., Sect. A* **569**, 685 (2006).
  - [7] L. U. Liang *et al.*, Successful high power acceleration of the HSC type injector for cancer therapy in IMP, [arXiv:1503.07326](https://arxiv.org/abs/1503.07326).
  - [8] M. Palmer *et al.*, *ICFA Beam Dynamics Newsletter* (Fermi National Accelerator Laboratory, Illinois, 2011), Vol. 55, p. 72.
  - [9] Y. Miyake *et al.*, Ultra slow muon microscopy by laser resonant ionization at J-PARC, MUSE, *Hyperfine Interact.* **216**, 79 (2013).

- [10] M. Bogomilov *et al.*, The MICE muon beam on ISIS and the beam-line instrumentation of the Muon Ionization Cooling Experiment, *J. Instrum.* **7**, P05009 (2012).
- [11] S. Artikova *et al.*, Simulation studies of low emittance muon re-acceleration for muon microscopy application, in *Proceedings of the 10th Annual Meetings of Particle Accelerator Society of Japan* (Particle Accelerator Society in Japan, Tokyo, Japan, 2013), p. SAP045.
- [12] G.W. Bennett *et al.*, Final report of the E821 muon anomalous magnetic moment measurement at BNL, *Phys. Rev. D* **73**, 072003 (2006).
- [13] J-PARC E34 conceptual design report, 2011 (unpublished).
- [14] G. A. Beer *et al.*, Enhancement of muonium emission rate from silica aerogel with a laser-ablated surface, *Prog. Theor. Exp. Phys.* (2014) 091C01.
- [15] P. Bakule, Y. Matsuda, Y. Miyake, K. Nagamine, M. Iwasaki, Y. Ikedo, K. Shimomura, P. Strasser, and S. Makimura, Pulsed source of ultra low energy positive muons for near-surface  $\mu$ SR studies, *Nucl. Instrum. Methods Phys. Res., Sect. B* **266**, 335 (2008).
- [16] Y. Kondo *et al.*, High-power test and thermal characteristics of a new radio-frequency quadrupole cavity for the Japan Proton Accelerator Research Complex linac, *Phys. Rev. ST Accel. Beams* **16**, 040102 (2013).
- [17] M. Otani *et al.*, Demonstration of muon acceleration and cavity design of the muon LINAC for J-PARC E34, in *Proceedings of the 12th Annual Meetings of Particle Accelerator Society of Japan* (Particle Accelerator Society in Japan, Tokyo, Japan, 2015), p. WEOM02.
- [18] G. Clemente *et al.*, Development of room temperature crossbar-H-mode cavities for proton and ion acceleration in the low to medium beta range, *Phys. Rev. ST Accel. Beams* **14**, 110101 (2011).
- [19] U. Ratzinger, CERN Yellow Report No. 2005-003, p. 351, 2005.
- [20] E. Nolte *et al.*, The Munich heavy ion postaccelerator, *Nucl. Instr. Meth.* **158**, 311 (1979).
- [21] N. Hayashizaki and M. Yoshida, Development of low energy muon linac, in *Proceedings of the 11th Annual Meetings of Particle Accelerator Society of Japan* (Particle Accelerator Society in Japan, Tokyo, Japan, 2014), p. SUP043.
- [22] U. Ratzinger, A low beta RF linac-structure of the IH-type with improved radial acceptance, in *1988 Linear Accelerator Conference Proceedings* (Jefferson Lab, Newport News, Virginia, USA, 1988), p. MO3-55.
- [23] S. S. Kurennoy *et al.*, H-mode accelerating structures with permanent-magnet quadrupole beam focusing, *Phys. Rev. ST Accel. Beams* **15**, 090101 (2012).
- [24] R. A. Jameson, Practical design of alternating-phase-focused linacs, [arXiv:1404.5176](https://arxiv.org/abs/1404.5176).
- [25] T. P. Wangler, *RF Linear Accelerators* (Wiley, New York, 2011).
- [26] D. A. Swenson, LANL internal Report No. MP-3/DAS-1, 1976.
- [27] W. D. Kilpatrick, Criterion for vacuum sparking designed to include both rf and dc, *Rev. Sci. Instrum.* **28**, 824 (1957).
- [28] T. J. Boyd Jr., Los Alamos Group AT-1 Report No. AT-1:82-28, 1982.
- [29] P. E. Gill *et al.*, Technical Report No. SOL 86-6, Revised June 4, 2001.
- [30] CST Studio Suite, Computer Simulation Technology (CST), <https://www.cst.com/products/CSTMWS>.
- [31] General Particle Tracer, Pulsar Physics, <http://www.pulsar.nl/gpt/>.
- [32] Y. Kondo *et al.*, Simulation study of muon acceleration using RFQ for a new muon g-2 experiment at J-PARC, in *Proceedings of the 6th International Particle Accelerator Conference* (Jefferson Lab, Newport News, Virginia, USA, 2015), p. THPF045.
- [33] K. R. Crandall and D. P. Rustoi, Los Alamos Report No. LA-UR-97-886, 1997.
- [34] Los Alamos Accelerator Code Group (LAACG), LANL, Los Alamos, <http://www.laacg.lanl.gov>.